Local structure in BaTiO_{3}-BiScO_{3} dipole glasses

I. Levin, V. Krayzman, J. C. Woicik, F. Bridges, G. E. Sterbinsky, T-M. Usher, J. L. Jones, and D. Torrejon

Phys. Rev. B **93**, 104106 — Published 14 March 2016
DOI: 10.1103/PhysRevB.93.104106

Local Structure in $BaTiO_3$-$BiScO_3$ Dipole Glasses

I. Levin[1*], V. Krayzman[1], J. C. Woicik[1], F. Bridges[2], G. E. Sterbinsky[3], T-M. Usher[4], J. L. Jones[4], D. Torrejon[5]

[1]Materials Measurement Science Division, National Institute of Standards and Technology, Gaithersburg MD 20899

[2]Department of Physics, University of California, Santa Cruz, CA

[3]Advanced Photon Source, Argonne National Laboratory, Argonne, IL

[4]Department of Materials Science and Engineering, North Carolina State University, Raleigh, NC

[5]Department of Mathematical Sciences, George Mason University, Fairfax, VA

[*]igor.levin@nist.gov

Abstract

Local structures in cubic perovskite-type $(Ba_{0.6}Bi_{0.4})(Ti_{0.6}Sc_{0.4})O_3$ solid solutions which exhibit reentrant dipole glass behavior have been studied with variable-temperature X-ray/neutron total scattering, extended X-ray absorption fine structure, and electron diffraction methods. Simultaneous fitting of these data using a Reverse Monte Carlo algorithm provided instantaneous atomic configurations which have been used to extract local displacements of the constituent species. The smaller Bi and Ti atoms exhibit probability density distributions which consist of 14 and 8 split sites, respectively. In contrast, Ba and Sc feature single-site distributions. The multi-site distributions arise from large and strongly anisotropic off-center displacements of Bi and Ti. The cation displacements are correlated over a short range, with a correlation length limited by chemical disorder. The magnitudes of these displacements and their anisotropy, which are largely determined by local chemistry, change relatively insignificantly on cooling from room temperature. The structure features a non-random distribution of local polarization with low-dimensional polar clusters that are several unit cells in size. *In situ* measurements of atomic pair-distribution function under applied electric field were used to study field-induced changes in the local structure; however, no significant effects besides noticeable lattice expansion in the direction of the field could be observed up to electric-field values of 4 kV/mm.

Introduction

Perovskite-like solid solutions between $BaTiO_3$ and $BiMO_3$ (M=Sc, $Mg_{½}Ti_{½}$, $Zn_{½}Ti_{½}$) exhibit dielectric properties promising for use in high-energy high-temperature capacitors for SiC-based power electronic inverters [1-6]. $BaTiO_3$, a classical ferroelectric compound, undergoes a sequence of phase transitions on cooling from a high-temperature paraelectric phase to ferroelectric tetragonal, orthorhombic, and finally rhombohedral polymorphs. The Bi-based end-members are unstable at ambient conditions and can be synthesized only using high pressures. The structures of $BiScO_3$ [7] and $BiMg_{½}Ti_{½}O_3$ [8] combine anti-polar patterns of Bi displacements (distinct in the two compounds) with octahedral rotations. In contrast, $BiZn_{½}Ti_{½}O_3$ crystallizes with a polar, strongly distorted tetragonal structure [9].

In (1-x)$BaTiO_3$-$x$$BiScO_3$ solid solutions, the ferroelectric transitions are rapidly suppressed with increasing x. According to the published X-ray diffraction data (XRD) [10, 11] the tetragonal ferroelectric phase is preserved up to $x\approx0.1$, whereas for higher x, a non-ferroelectric cubic phase is stabilized. This cubic phase, which persists up to a solubility limit ($x\approx0.45$), exhibits a large dielectric constant with a temperature dependence exhibiting strong frequency dispersion; for $x\geq0.3$, this dependence becomes extraordinarily flat over a broad temperature range [10]. Analyses of the dielectric data using Arrhenius and Vogel-Fulcher models yielded activation energies of 0.2-0.3 eV [10], which are significantly higher than those encountered in typical relaxor ferroelectrics. Overall, the dielectric response of these materials is consistent with dipole-glass behavior. The $BaTiO_3$-$BiMg_{½}Ti_{½}O_3$ and BaTiO3-$BiZn_{½}Ti_{½}O_3$ systems exhibit similar properties.

At lower temperatures, cubic samples of $BaTiO_3$-$BiScO_3$ yield polarization hysteresis loops showing small values of the remnant polarization (P_r<10 mC/cm^2) and large coercive fields (50 to 250 kV/cm) [10, 12, 13]. The dependence of P_r on temperature is non-monotonic, with a maximum which occurs below the glass transition temperature (T_{DG}) derived from dielectric measurements. Upon further cooling, P_r decreases to zero – an effect that has been attributed to appearance of a reentrant dipole-glass state [10-13]. The exact mechanisms underlying the dielectric relaxation and reentrant dipole-glass properties remain uncertain.

Recently, Krayzman *et al.* [14] communicated selected results of a study of the local structures in $BaTiO_3$-$BiScO_3$ dielectrics using the Reverse Monte Carlo (RMC) method. The instantaneous atomic displacements determined by simultaneous fitting of multiple types of experimental data were used to develop a qualitative model that related the structural features to the dielectric properties and reentrant dipole-glass behavior. In particular, the dielectric relaxation in $BaTiO_3$-$BiScO_3$ was attributed to a correlated rattling motion of Bi and Ti over their corresponding split sites identified from the RMC analysis. The current report provides a complete account of this structural work, including discussion of variable-temperature diffraction and spectroscopic data along with the results of *in situ* measurements of an atomic pair-distribution function (PDF) under electric field. Additionally, this paper presents a new approach for measuring piezoelectric/electrostrictive strain at the nanoscale.

Experimental

(1-x)$BaTiO_3$-x$BiScO_3$ (BBTS) samples with *x*=0.2 and *x*=0.4 were prepared using solid-state methods. Powders of $BaCO_3$, Bi_2O_3, TiO_2 and Sc_2O_3 were mixed by grinding with an agate mortar and pestle under acetone, pelletized, and calcined at 950 °C for 10 h. The calcined powder was reground, pelletized, and sintered at 1100 °C for 5 h in air. Samples were characterized using XRD in a powder diffractometer equipped with an incident beam monochromator (Cu $K\alpha_I$ radiation) and a solid-state position sensitive detector. For both samples, the XRD patterns were indexable with a cubic perovskite *Pm3m* unit cell. For *x*=0.4, relatively narrow and symmetric peaks were obtained, consistent with a single cubic phase (Fig. 1a). In contrast, for *x*=0.2 (Fig. 1b), the peaks were broad and asymmetric, with shoulders likely attributable to inhomogeneity, with chemically-distinct regions featuring different lattice parameters/distortions; these results are consistent with previous XRD studies of the BBTS system [11]. Repeated heating of this sample at 1100 °C and 1200 °C produced no significant changes. Additional heating at 1400 °C (5 h) eventually yielded more symmetric peaks albeit with broad bases (Fig. 1b); however, at this temperature Bi volatility becomes likely. Considering a heterogeneous structure of the *x*=0.2 sample, further studies were focused on the *x*=0.4 composition.

Neutron total scattering measurements were performed using the NPDF instrument at the Lujan Center for Neutron Scattering (Los Alamos National Laboratory). The sample powder was loaded in a vanadium container mounted on the top loading displex. The total scattering data, recorded at several temperatures between 15 K and 300 K, were processed using the PDFgetN software [15] to extract the normalized scattering function *S*(*Q*) and its corresponding pair-distribution function (PDF) G(*r*). A $Q_{\max}$ value was selected at 30 $Å^{-1}$.

Variable-temperature X-ray total scattering was measured between 80 K and room temperature at the 11-ID-B beamline of the Advanced Photon Source (Argonne National Laboratory) using an incident beam energy of 86.7 keV (λ=0.143 Å) and a two-dimensional amorphous silicon detector. The sample was mounted in a kapton capillary with temperature control achieved using a cryostream system. *In situ* measurements of X-ray total scattering during the application of a static electric field were performed at room temperature using the same beamline set up and the electric-field loading stage, as described in Ref. 16. The sample, a ceramic bar ≈0.8 mm × 0.8 mm × 5 mm covered with silver electrodes on opposing sides, was immersed in the insulating liquid. The data were collected while increasing the electric field amplitude in increments of 0.33 kV/mm; the direction of the field was set vertical. In all cases, the diffraction patterns were reduced using the program Fit2D to obtain one-dimensional traces of intensity as a function of the scattering vector $\boldsymbol{Q}$. For the field-dependent measurements, one-dimensional traces corresponding to $\boldsymbol{Q}$ oriented parallel to the field were extracted by integrating a diffraction image over an azimuthal sector of 20° centered on the vertical direction. The intensity data, corrected for polarization, were further processed using PDFGetX3 [17] to derive the *S*(*Q*) and *G*(*r*). A previous study [16] has shown that the directional *G*(*r*) obtained using the sine Fourier transform of *S*(*Q*) is close to the *G*(*r*) constructed using a more accurate spherical-harmonics approach. A $Q_{\max}$ value was set at 25 $Å^{-1}$. Background scattering from the insulating liquid was measured separately and subtracted during data reduction.

Extended X-ray absorption fine structure (EXAFS) was measured for the *L_3* and K edges of Bi (13419 eV) and Sc (4492 eV), respectively. Additionally, we measured a pre-edge structure for the Ti *K*-edge (4966 eV); measurements of Ti EXAFS were precluded by the overlap between the Ti *K* and Ba L_3 (5247 eV) edges. Variable-temperature measurements of Bi and Ti were performed at the National Institute of Standards and Technology (NIST) beamline X23A2 of the National Synchrotron Light Source (Brookhaven National Laboratory). A thin layer of the sample powder was dispersed on a thin aluminum foil mounted on a displex, which was used to control temperature. The measurements for the Bi L_3 and Ti *K* edges were executed in transmission and fluorescence, respectively, at a series of temperatures between 15 K and 300 K. Sc *K*-edge EXAFS was measured using beamline 4-3 of the Stanford Synchrotron Radiation Lightsource. The sample powder for these measurements was dispersed on sticky tape and mounted on a helium flow cryostat. The measurements were performed in transmission at a series of temperatures between 4 K and 300 K. All X-ray absorption data were processed using Athena. Initial fitting was accomplished using Artemis [18]. Scattering amplitudes and phases were calculated using FEFF8 [19].

Electron diffraction patterns and atomic-resolution high-angle annular dark field imaging were collected using a conventional transmission electron microscope (TEM) (200 kV) and a scanning TEM (STEM) (300 kV) equipped with a probe aberration corrector, respectively. The samples were prepared by crushing the sintered pellets in ethanol and dispersing the resulting powder on lacey-carbon coated copper grids (ion thinning was avoided because of noticeable artefacts). Variable-temperature electron diffraction data were collected using a liquid-nitrogen-cooled sample stage.

Rietveld refinements were performed using the GSAS software package [20]. In these refinements, a cubic *Pm3m* structural model was adopted with the atoms located in the following positions: Ba/Bi (0,0,0), Ti/Sc (½,½,½), and O (½,½, 0). Anisotropic atomic displacements parameters were refined for the oxygen positions.

Local-structure refinements were accomplished using the RMCProfile software modified to enable simultaneous fitting of multiple types of data [21-22]. In the present refinements a total of 17 datasets were used, which included: a neutron total scattering function and its corresponding PDF, a neutron Bragg profile, an X-ray total scattering function and its corresponding PDF, Bi and Sc EXAFS datasets, single-crystal diffuse-scattering patterns representing {221}, {331}, and {112} sections of reciprocal space (with equivalent permutations of the *hkl* indexes), and the magnitude of Ti off-centering determined from the intensity of the pre-edge peak in the Ti *K*-edge X-ray absorption spectra (XAS). The refinements were performed for 300 K and 100 K, which are above and below the glass transition temperature, respectively, for this composition; T=100 K was the lowest temperature for which the X-ray PDF and electron diffraction data were available. During the fit, the calculated X-ray PDF was determined as the Fourier transform of the corresponding calculated total-scattering function to account for the *Q*-dependence of the atomic X-ray scattering cross-sections. The fitted *r*-ranges for the Bi and Sc EXAFS data were from 1.1 Å to 3.1 Å and from 0.9 Å to 2.25 Å for Bi and Sc, respectively; all the scattering paths (metal-oxygen, metal-metal) that fall within these ranges were included in the fit. The weights assigned to the individual datasets were adjusted automatically according to an algorithm, outlined in Appendix A, which ensured that all the residuals eventually decreased to small preset values.

The atomic configurations used to fit the data contained 16 × 16 × 16 perovskite unit cells with a total of 20,480 atoms. Different starting configurations were tried to test the uniqueness of structural characteristics calculated from the refined atomic coordinates. In particular, we tried models with several distributions of cations corresponding to random and non-random (ordering, clustering) cases. The models featuring random distributions provided noticeably better fits and will be presented here. Also, the HAADF images in STEM, which emphasize heavy Bi (Z=83) and Ba (56) atoms, revealed no signs of extended deviations from random distributions.

Results & Discussion

Analyses of $(Ba_{0.6}Bi_{0.4})(Ti_{0.6}Sc_{0.4})O_3$ using individual measurement techniques

Fig. 2 presents temperature dependences of the lattice and atomic displacement parameters (ADP) as determined from Rietveld refinements using the neutron diffraction data. No discernable anomalies in both trends can be observed. The ADPs for the Ba/Bi sites are relatively large thus suggesting significant Bi displacements off the average positions (large Ba cations are unlikely to be displaced). All the ADPs decrease monotonically but relatively weakly with decreasing temperature which indicates their largely quasi-static nature. Cooling the sample from 300 K to 15 K leaves the widths of the Bragg peaks (in the high-resolution detector bank) unchanged (Fig. 3), thus ruling out lattice distortions beyond the resolution of the instrument ($\Delta d/d \approx 0.0015$).

As discussed previously [14], strongly dissimilar ionic sizes and charges of the ions occupying both the cube-octahedral A (Ba, Bi) and octahedral B (Ti, Sc) sites should result in local deviations from cubic symmetry. In particular, the presence of large Ba^{2+} (R_{Ba}=1.61 Å) and Sc^{3+} (R_{Sc}=0.745 Å) results in oversized oxygen cages for Bi^{3+} (R_{Bi}=1.31 Å) and Ti^{4+} (R_{Ti}=0.605 Å) which, therefore, should be displaced to relieve the large tensile strains in the Bi-O and Ti-O bonds. A PDF obtained from the neutron total scattering (Fig. 4a) confirms this supposition: the cubic model provides a satisfactory fit to this PDF for r>5 Å, but at shorter distances notable differences are observed. One evident source of discrepancy is the difference between the short Ti-O (a negative peak at 1.75 Å) and longer Sc-O (a positive peak at 2.2 Å) bond lengths. However, a strong overlap of peaks corresponding to different atomic pairs precludes an intuitive interpretation of the PDF. Cooling the sample to 15 K causes sharpening of the PDF peaks (Fig. 5); however, the changes are fairly small and display no anomalies. Fitting the PDF using the cubic model and a box-car approach (fitted Δr=5 Å, step=1 Å) indicates that significant deviations from the average structure are confined to 8 Å at the most (i.e. 2 unit cells), as expected for a solid solution (Fig. 4b). These results suggest that polar clusters in this system, if present, would be limited to 2-3 unit cells in diameter.

Bi EXAFS is dominated by the contribution from the Bi-O distances (Fig. 6). The 300 K data can be fitted satisfactorily using a single Bi-O distance of 2.230(8) Å having a multiplicity of 3 (e.g., Bi displacements along $\langle 111 \rangle$) and a Debye-Waller (D-W) factor of $\approx$0.007(1) Å^2. This short Bi-O distance is typical for strongly off-centered Bi, as observed in other perovskites [23-26] and in disordered pyrochlores [27]. Both the Bi-O distance and its D-W factor decrease only slightly on cooling (the changes are systematic but fall within the standard uncertainty) as might be expected for a strongly covalent chemical bond. These results are consistent with the weak changes of the ≈2.2 Å peak in the X-ray PDF (Fig. 5b), which arise primarily from the short Bi-O distances.

Sc EXAFS (Fig. 7) data are described well assuming 6-fold coordination with a Sc-O distance of ≈2.102(5) Å, which yields a bond valence sum of ≈3.03 valence units (v.u), close to the formal value. The Debye-Waller (D-W) factor for the Sc-O distance is 0.007(1) $Å^2$. The Sc-O distance and its D-W factor decrease by only ≈0.01 Å and ≈0.002 $Å^2$, respectively, on cooling from 300 K to 15 K.

The intensity of the Ti pre-edge peak (Fig. 8) is proportional to the squared value of the Ti off-centering (δ_{Ti}^2) within the oxygen octahedra (this off-centering depends on both the Ti and O displacements) [28]. After accounting for the effects of changes in the lattice parameter on the pre-edge peak intensity, in BBTS we obtain δ_{Ti}=0.27 Å which is larger than δ_{Ti}=0.22 Å in $BaTiO_3$. This difference contrasts with the smaller unit-cell volume observed in BBTS suggesting that Ti off-centering might be enhanced by the Bi displacements. Cooling the sample to 15 K produced no measurable difference in the intensity of the pre-edge peak (the sample was additionally measured in fluorescence by mounting it on a sapphire disk provided with the displex to ensure that the temperature on the sample was indeed close to its nominal value). This striking lack of change suggests that the off-centering is dominated by a static component.

Electron diffraction patterns of BBTS exhibit pronounced diffuse scattering which mostly represents traces of diffuse {111} sheets (Fig. 9). This scattering has been attributed to chain-like correlations of A- and B-cation displacements along $\langle 111 \rangle$ directions [4, 29]. The relevant correlation length, ξ, can be estimated from the width of the diffuse streaks. Commonly, the diffuse-intensity profiles across the streaks adopt a Lorentzian shape which corresponds to the Ornstein-Zernike dependence $e^{-r/\xi}$ of the correlation strength on distance r, as encountered, for example, in $BaTiO_3$ (Fig. 10a). In this case, $1/\xi$ is equal to a half-width at half-maximum of the diffuse-intensity peak. However, in BBTS (Fig. 10b), the diffuse-intensity profile acquires a Gaussian rather than a Lorentzian shape, which indicates that the correlation strength decreases faster with distance than described by the Ornstein-Zernike dependence. This more rapid decay is attributed to the presence of chemical disorder on both cation sites, which limits the spatial extent of correlations. The distance that corresponds to one standard deviation of the real-space Gaussian distribution derived from the diffuse-intensity profile in BBST is ξ≈6.5 Å. The diffuse scattering remained largely unchanged upon cooling the sample to 100 K (nominal) (Fig. 9). Apparently, the correlation length is fixed by the chemical disorder.

Simultaneous RMC fitting of combined data

The room-temperature experimental and calculated signals obtained using RMC refinements are compared in Fig. 11. The EXAFS data (Fig. 11e, f) were critical for differentiating between the coordination environments of species sharing the same crystallographic sites. Atomic configurations obtained without the X-ray total scattering or electron diffuse scattering included in the fit were evidently incorrect since they could not reproduce the respective omitted signals. Moreover, without including the electron diffuse scattering, we could not even fit the total-scattering data satisfactorily, presumably because of the difficulties with reconciling the local and average structures in the absence of the correct interatomic correlations (i.e., the refinements converge to a local minimum). Fitting the data collected at 100 K also resulted in satisfactory agreement of the calculated and experimental signals; importantly, the key differences between the data measured at 300 K and 100 K (e.g., sharpening of the PDF peaks on cooling) were reproduced (Fig. 12).

Selected partial PDFs reconstructed using the RMC refinements are displayed in Fig 13. As expected, the Ti-O bond lengths are split, reflecting the Ti off-centering relative to oxygen. In contrast, the Sc-O bond lengths exhibit a unimodal distribution. The Bi-O partial (determined almost exclusively by the EXAFS data) reveals the existence of short Bi-O distances at ≈2.2 Å featuring a narrow distribution and a multiplicity of ≈3. The distribution of the Ba-O bond lengths is represented by a single symmetric, albeit relatively broad peak at ≈2.84 Å, which corresponds to a Ba BVS of 2.7 v.u.; thus, the Ba-O bonds are strongly compressed, as it has been observed in $BaTiO_3$. The partial PDFs changed relatively insignificantly between 300 K and 100 K, apart from the Ti-O distance distribution. The separation between the two split Ti-O distances is noticeably smaller at 100 K, which appears to be at odds with the constant magnitude of the Ti off-centering at 300 K and 100 K; this apparent discrepancy is reconciled by changes in the magnitude and anisotropy of the oxygen displacements.

The average volume of $[TiO_6]$ in BBTS is smaller compared to that in $BaTiO_3$, which contrasts with the larger Ti off-centering in the solid solutions (Fig. 14). The range of Ti-O distances within individual octahedra is considerably larger and distributed more broadly compared to the same characteristics for $[ScO_6]$. The local volumes of $[TiO_6]$ and $[ScO_6]$ decrease and increase, respectively, with increasing number of nearest Bi atoms, whereas these trends are reversed for the off-centering of Ti and Sc within their respective octahedra. These results further support the inference that large Bi displacements enhance the Ti off-centering relative to $BaTiO_3$.

The instantaneous probability density distributions (PDD) of both Bi and Ti feature split sites and the overall character of these distributions is retained on cooling from 300 K to 100 K (Fig. 15). The 3-D PDD of Bi consists of 14 well-separated sites displaced along 8 ⟨111⟩ (≈75 % and 50 % of the total number of atoms at 300 K and 100 K, respectively) and 6 ⟨100⟩ directions off the ideal average A-site position, whereas the PDD of Ti is consistent with the 8 overlapping sites shifted along ⟨111⟩. A strong preference for Bi to be displaced along either ⟨111⟩ or ⟨100⟩ is evident from the stereographic-projection plots of the probability density for the displacement directions. (Fig. 16). For Bi, the distinct "⟨111⟩" sites are separated by ≈0.8 Å at both 300 K and 100 K, whereas the distance between nearest "⟨111⟩" and "⟨100⟩" sites is ≈0.5 Å, and is somewhat larger at 100 K. Bi displacements along several preferred directions have also been reported in $Na_{½}Bi_{½}TiO_3$ [24]. Likely, specific directions of Bi displacements are determined by local chemistry; however, these correlations were unobservable in the presently refined configurations. While the Ti PDD is similar that observed in $BaTiO_3$, the ⟨100⟩ chain-like correlations among the Ti displacements, which exist in the end compound, appear to be destroyed in the cubic BBTS solid solution, as evidenced by the absence of significant {100} diffuse sheets. The Ti site splitting of ≈0.16 Å is comparable to the intra-well spread of displacements (0.15 Å). The PDDs of the larger Ba and Sc atoms are unimodal with their corresponding spreads of displacements similar to those observed for the individual split sites of Bi and Ti, respectively. The PDD of oxygen (Fig. 17) acquires a strongly anisotropic shape indicating preferential oxygen displacements along ⟨110⟩ directions: oxygen atoms shift strongly toward the neighboring Bi atoms to form short Bi-O bonds, as also reflected in large negative correlation parameters for the Bi and O displacements (≈-0.3).

The spread of PDDs for Ba, Sc, Ti, and O decreases on cooling from 300 K and 100 K. For Bi, the "⟨100⟩" sites are significantly more displaced from the ideal A-site positions at 100 K, whereas the "⟨111⟩" sites remain relatively unchanged. The site splitting for Ti at 100 K appears to be smaller than that at 300 K, which contrasts with the temperature-independent off-centering of Ti relative to oxygen; as discussed above, this discrepancy is accounted for by changes in the anisotropy of the oxygen displacements.

Knowledge of spatial correlations among polar atomic displacements is critical for understanding the dielectric behavior in this class of materials. The RMC method of fitting data [30, Appendix A] relies on acceptance or rejection of random atomic moves, depending on their effect on a misfit between experimental and calculated signals. Therefore, RMC-refined configurations typically represent the most disordered cases consistent with the experimental data, thereby providing information on the minimum level of correlations that exist in a given system. The correlation parameters, $c_{ij}(r)$, for atomic displacements were calculated using a common approach described in Ref. 22. As expected from the presence of diffuse-scattering sheets, the cation (A and B) displacements are correlated (Fig. 18) with the correlations decaying to zero at distances of ≈14 Å; the differences between the correlations observed at 300 K and 100 K appear to be statistically insignificant. Particularly strong positive correlations (correlation parameter ≈0.5) exist among the displacements of nearest Bi and Ti cations (not shown in the plot) mediated by the oxygen ions.

Local Polarization and Polar Nanoregions

We used atomic displacements and Born effective charges to calculate values of polarization for individual unit cells in the refined configurations (Fig. 19a). In the absence of computational work for BBTS, sensible values of these charges (Z_{Bi}=5, Z_{Ba}=2.75, Z_{Sc}=4, Z_{Ti}=7, $Z_{O\|}$=-4.65, $Z_{O\perp}$=-2.4) were adopted from the literature on related compositions [31-34]. The distribution of the local polarization differed for centers of the unit cells selected at A or B-sites; however, the first moments of these distributions were similar. Fig. 19a displays a {110} slice, 3 unit cells thick, through the refined atomic configuration with the arrows representing projections of the unit-cell polarizations (centered on the A-sites and averaged over slice thickness) onto the slice plane. Clearly, identifying regions of local order from visual examination of this type of figures is challenging. We developed an automated procedure to search for polar clusters which consist of at least two unit cells. According to our definitions, the neighboring unit cells belong to the same cluster if the directions of their polarization vectors fall within the specified tolerance angle, α. The results obtained for the refined atomic configurations were compared to those for a reference configuration which featured the same polarization vectors but without spatial correlations. This analysis (Fig. 19b) revealed a significantly non-random distribution of cluster sizes in BTBS; the differences are particularly noticeable for the clusters that consist of 3 or more unit cells. As can be seen from the 3-D rendering of the refined configuration (Fig. 19c), the polar clusters (≥ 4 unit cells) are one and two-dimensional.

Structural changes under electric field: In situ PDF measurements

Application of an electric field, ***E***, reduces the symmetry of the sample, and the diffracted intensities become dependent on the angle β between the scattering vector ***Q*** and field ***E***. One-dimensional X-ray total-scattering patterns were extracted from the 2-D diffraction images so that $\beta \approx 0$. Each Bragg peak in these patterns arises from a distinct population of crystallites having its corresponding ***Q*** parallel to ***E***. These patterns were processed to deduce the PDFs, which represent distributions of interatomic distances in the sample along the direction parallel to ***E***. No discernable differences can be observed by eye between such directional PDFs at E=0 and E=4 kV/mm.

Quantitative evaluation of the difference curves for the variable-field data was performed by defining the residual as [16]

$$R = \frac{\sum |G(r+\delta r)_E - G(r)_{E=0}|}{\sum |G(r)_E|},$$

where $G(r)_E$ and $G(r)_{E=0}$ refer to the PDFs under the electric field $E \neq 0$ and E=0, respectively; summation is performed over a specified r-range. This R-value was calculated using a box-car method with a sampling range of ±0.25 and a step size of 0.5 Å. The effects of peak shift, δr, and peak broadening on R were also separated. For each box position, $G(r)_E$ was shifted along the r-axis relative to $G(r)_{E=0}$ to minimize R and the resulting values of δr and R were plotted against r.

Applying this new approach to the data reveals a systematically increasing upshift of the PDF peaks with increasing r, which indicates lattice expansion parallel to the field (Fig. 20a). (The S(Q) also revealed small downshifts of Bragg peaks having ***Q*** parallel to ***E***). Fitting a straight line to these data in the range 20 Å<r<50 Å under a constraint of the zero shift at r=0 Å yields a value of strain ε at a given field. Fig. 20b presents the dependence of ε on E for BBTS. (Analysis of the directional PDF perpendicular to the field revealed lattice contraction, which, however, was too small to be reliably quantified). For comparison, we performed a similar analysis for $SrTO_3$ and $BaTiO_3$. The strain in BBTS is about 5 times larger than that in $SrTiO_3$, and about 5 times smaller compared to ε in $BaTiO_3$. This kind of analysis provides a way to measure intrinsic electrostrictive and piezoelectrics coefficients in polycrystalline materials over the mesoscale. The effect of an electric field on peak broadening in $G(r)$ as a function of r was evaluated by considering an integral of the 2nd derivative of $G(r)$ squared (Fig. 20c). For r<20 Å the PDF peaks appear to broaden under the field, whereas for r>20 Å the opposite trend is observed (Fig. 20d); however, overall, the effects are small, somewhat inconsistent for different E-values, and, therefore, difficult to interpret.

Detailed analysis of contributions from the refined partials indicates that visible features in the total X-ray PDF mostly reflect interatomic distances involving Ba, whereas those associated with Bi are compensated in the sum. The only clearly recognizable signature of Bi in the X-ray PDF is the peak at ≈2.2 Å, which represents the short Bi-O distances along the direction parallel to the field. The split short and long Bi-Ti/Bi-Sc distances produce no discernable features, as they are largely compensated by the contributions from other (Bi-O, Ba-Ti/Sc) partials. In the case of an electric field causing Bi to switch sites to increase the occupancy of those more favorably aligned with ***E***, the fraction of short Bi-O bonds observed along ***E*** should increase. The absence of changes in the peak representing such short distances suggests that no significant site switching is taking place for the electric fields applied in this study (4 kV/mm); that is, Bi atoms remain confined to their original wells. Indeed, as suggested in Ref. 10, significantly higher fields are required to activate the switching mechanism. For example, electric fields up to ≈55 kV/mm have been used to yield hysteresis loops that displayed non-zero remnant polarization in a certain temperature range.

Conclusions

According to the present analysis, cubic single-phase 0.6$BaTiO_3$-0.4$BiScO_3$ features a nearly random distribution of metal species with strong off-center displacements of Bi and Ti correlated over a short distance (≈10 Å). These displacements are strongly anisotropic thus yielding split-site probability density distributions for both cations. In particular, Bi is displaced by ≈0.5 Å along both the $\langle 111 \rangle$ and $\langle 100 \rangle$ directions; a fraction of the $\langle 100 \rangle$ displacements increases with decreasing temperature. The minimal site separation between the split Bi sites is larger at 100 K compared to room temperature, which is consistent with the absence of site switching below the dipole-glass transition temperature, even under large electric fields – an effect that has been proposed to be the origin of the reentrant dipole-glass state [14]. The Ti atoms are preferentially displaced along $\langle 111 \rangle$ directions by ≈0.08 Å. The structure features mostly low-dimensional (1-D and 2-D) polar clusters, several unit cells in size, present in substantially larger numbers than expected for a random distribution of the unit-cell polarization vectors. The size distribution of these clusters changes insignificantly between 300 K and 100 K.

The $BaTiO_3$-$BiMO_3$ systems differ from common relaxor ferroelectrics ($PbMn_{1/3}Nb_{2/3}O_3$, $Na_{1/2}Bi_{1/2}TiO_3$, $Ba(Zr,Ti)O_3$) [35-37] by the mixtures of displacively active and blocking species on both A- and B-sites. This “double-site” chemical disorder frustrates local polarization, limiting the polar order to just a few unit cells down to low temperatures. Switching of the local polarization in polar clusters of the kind identified in the present study is equivalent to a correlated switching of Bi and Ti from one of their respective split sites to another. As suggested previously, such double-ion rattling motion can explain the dielectric relaxation observed in cubic $BaTiO_3$-$BiScO_3$ compositions. A large separation between the split Bi sites, determined by both the magnitude of the Bi displacements and their anisotropy results in high activation energies for the relaxation observed in dielectric measurements, whereas chemical disorder accounts for a broad distribution of the relaxation times. A model of multiple rattling ions in perovskites, suggested by the present structural measurements in $BaTiO_3$-$BiScO_3$ solid solutions, merits further exploration as a tool for tailoring dielectric properties.

Figure Captions

Fig. 1: Traces of the 200 peak in X-ray diffraction patterns of (a) $Ba_{0.6}Bi_{0.4}Ti_{0.6}Sc_{0.4}O_3$ heat-treated at 1100 °C and (b) $Ba_{0.8}Bi_{0.2}Ti_{0.8}Sc_{0.2}O_3$ heat-treated at 1100 °C, 1200 °C, and 1400 °C.

Fig. 2: Temperature dependences of the (a) lattice parameters and (b) atomic displacement parameters (ADPs) for $Ba_{0.6}Bi_{0.4}Ti_{0.6}Sc_{0.4}O_3$ obtained by Rietveld refinement using neutron powder diffraction data.

Fig. 3: Traces of the 220 Bragg peaks in the neutron diffraction patterns recorded at 300 K and 15 K. The peaks have been shifted and rescaled to compare the broadening.

Fig. 4: (a) Experimental (red) and calculated (blue) neutron PDFs for $Ba_{0.6}Bi_{0.4}Ti_{0.6}Sc_{0.4}O_3$; the difference curve is shown in green. The calculated pattern was obtained by fitting a cubic perovskite model to the data over the entire *r*-range. (b) Dependence of the *R*-factor (describing the quality of fit) on distance, obtained using the box-car method.

Fig. 5: Temperature dependences of the (a) neutron and (b) X-ray PDFs. The neutron and X-ray scattering data were collected over the temperature ranges of 300 K to 15 K and 300 K to 80 K, respectively.

Fig. 6: Temperature dependence of the Bi EXAFS in (a) *k*- and (b) *r*-spaces (from 300 K to 15 K). The *k*-space data has been multiplied by *k* prior to the Fourier transform. The *k*-range used in the Fourier transform was from 3.0 $Å^{-1}$ to 12.75 $Å^{-1}$.

Fig. 7: Temperature dependence of the Sc EXAFS in (a) *k*- and (b) *r*-spaces (from 300 K to 6 K). The *k*-space data has been multiplied by *k* prior to the Fourier transform. The *k*-range used in the Fourier transform was from 2.85 $Å^{-1}$ to 10.75 $Å^{-1}$. The upper limit for the *k*-range was determined by the overlap with the Ti K-edge.

Fig. 8: The pre-edge structure in the Ti K-edge X-ray absorption spectra recorded between 300 K and 15 K. All changes are within the line thickness. The room-temperature spectrum for $BaTiO_3$ (blue line) is superimposed as a reference. The inset shown a magnified view of the pre-edge peak which is related to the Ti off-centering.

Fig. 9: Selected area electron diffraction patterns recorded from $Ba_{0.6}Bi_{0.4}Ti_{0.6}Sc_{0.4}O_3$ at (a) 300 K and (b) 100 K in $\langle 221 \rangle$ zone-axis orientation. No significant differences in the diffuse scattering can be observed.

Fig. 10: Intensity profiles across the diffuse streaks in (a) $BaTiO_3$ (streaks passing through 003 reflections) and (b) $Ba_{0.6}Bi_{0.4}Ti_{0.6}Sc_{0.4}O_3$ (streaks passing through 3-30 reflections). Dots represent the experimental profiles. Red and blue lines correspond to the fits of these profiles using Gaussian and Lorentzian distributions, respectively.

Fig. 11: Experimental and calculated signals/patterns obtained using simultaneous RMC fitting of multiple datasets. (a) neutron PDF, (b) neutron S(Q), (c) X-ray PDF, (d) X-ray S(*Q*), (e) Bi EXAFS, (f) Sc EXAFS,

(g-i) electron diffuse scattering patterns in ⟨221⟩, ⟨331⟩, and ⟨122⟩ sections of reciprocal space, respectively. In figures (a-d) the red and blue traces correspond to the experimental and calculated data, respectively, whereas the green traces represent the residuals. The insets in (b) and (d) display magnified high *Q* portions of the diffraction patterns. In figures (e) and (f), the red and blue traces represent the experimental and calculated moduli of the EXAFS Fourier transforms (FT), respectively; the green and black lines correspond to the experimental and calculated imaginary parts of the FT. In figures (g-i), the left and right halves of each figure, separated by the white dashed line, correspond to the experimental and calculated patterns, respectively.

Fig. 12: Experimental (dots) and calculated (lines) neutron (a) and X-ray (b) PDFs for 300 K (red) and 100 K (blue).

Fig. 13: Selected partial PDFs for 300 K (solid line) and 100 K (dotted line) obtained using the RMC refinements. (a) Ti-O and Sc-O and (b) Ba-O and Bi-O partials. A small bump-like Ti-O peak at larger distances is most likely an artefact of the fit.

Fig. 14: Statistical distributions of the local [TiO_6] and [ScO_6] octahedral volumes (300 K). The average volume of the [TIO_6] octahedra in $BaTiO_3$ is indicated using a dashed vertical line.

Fig. 15: (a) The cation probability density distributions projected onto {100} planes at 300 K (right) and 100 K (left).

Fig. 16: Stereographic projections displaying the probability density distributions for directions of the Bi displacements at 100 K and 300 K. These distributions exhibit well-defined maxima for the ⟨111⟩ and ⟨100⟩ directions. The relative probability of ⟨111⟩ displacements is larger at 300 K.

Fig. 17: Probability density distributions of oxygen atoms projected onto {001} plane (a-b); (c-d) a {110} slice through this PDD.

Fig. 18: (a) A {110} slice through the refined configuration, 3 unit cells thick. Projections of atomic displacements onto the slice plane averaged over the slice thickness are indicated using colored arrows. (b) Dependence of the displacement correlation parameters c_{ij} for the A- and B-cations on distance. The correlation parameters are calculated for the AA, AB, and BB pairs.

Fig. 19: (a) a {110} slice through the refined configuration, 3 unit cells thick. Projections of the unit-cell polarization vectors, calculated using atomic coordinates and Born effective charges and averaged over the slice thickness, are indicated using arrows. (b) The number of polar clusters versus cluster size for a tolerance angle α=25®. Orange – a distribution calculated for the refined configuration. Dark red – a distribution obtained for a configuration with randomized locations of the unit-cell polarization vectors. (c) A 3-D rendering of the configuration box with the polar clusters, 4 unit cells in size or larger, indicated using colored dots. Each dot represents a single unit cell. The unit cells that belong to the same cluster have the same color.

Fig. 20: (a) dependence of the PDF peak shift δr on distance for *E*=4 kV/mm relative to *E*=0 at $\beta\approx 0$. The dashed straight line is used to highlight the trend. Clearly, the crystal lattice expands along the

direction of the field. (b) Dependence of the lattice expansion parallel to ***E*** on the magnitude of the field. The statistical uncertainties associated with linear fits to the data shown in (a) are within the symbol size. The origin of the kink at $E≈1.8$ kV/mm is unknown. (c) An integral of the second derivative of $G(r)$ squared as a function of distance for $E=4$ kV/mm (red line) and $E=0$ (blue line); this integral reflects the dependence of PDF peak broadening on distance. (d) A difference between the two curves in (c).

References

1. Ogihara, C. A. Randall, S. Trolier-McKinstry, J. Am. Ceram. Soc., 92 [1] 110-118 (2009)
2. D. H. Choi, A. Baker, M. Lanagan, S. Trolier-McKinstry, C. Randall, J. Am. Ceram. Soc., 96 [7] 2197-2202 (2013)
3. S. Wada, K. Yamamoto, P. Pulpan, N. Kumada, B. –Y. Lee, T. Iijima, C. Moriyoshi, Y. Kuroiwa, J. Appl. Phys., 108, 094114 (2010)
4. J. Wang, Y. Liu, Q. Li, K. Lau, R. L. Withers, Z. Li, Appl. Phys. Lett., 103, 042910 (2013)
5. E. A. Patterson and D. P. Cann, J. Am. Ceram. Soc., 95 [11], 3509-3513 (2012)
6. N. Triamnik, R. Yimnirun, J. Pokorny, D. P. Cann, J. Am. Ceram. Soc., 96 [10], 3176-3182 (2013)
7. A. A. Belik, T. Yokosawa, K. Kimoto, Y. Matsui, E. Takayama-Muromachi, Chem. Mater., 19 [7], 1679-1689 (2007)
8. D. D. Khalyavin, A. N. Salak, N. P. Vyshatko, A. B. Lopes, N. M. Olekhnovich, A. V. Pushkarev, I. I. Maroz, Y. V. Radyush, Chem. Mater., 1, 18, 5104 (2006)
9. M. R. Suchomel, A. M. Fogg, M. Allix, H. Hiu, J. B. Claridge, M. J. Rosseinsky, Chem. Mater., 18, 4987 (2006)
10. S. S. N. Bharadwaja, J. R. Kim, H. Ogihara, L. E. Cross, S. Trolier-McKinstry, C. A. Randall, Phys. Rev. B., 83 [2] 024106 (2011)
11. K. Datta and P. A. Thomas, J. Appl. Phys., 107, 043516 (2010)
12. H. Y. Guo, C. Lei, Z-G. Ye, Appl. Phys. Lett., 92 [17], 172901 (2008)
13. S. S. N. Bharadwaja, S. Trolier-McKinstry, L. E. Cross, C. A. Randall, Appl. Phys. Lett., 100 [2], 022906 (2012)
14. V. Krayzman, I. Levin, J. C. Woicik, F. Bridges, Appl. Phys. Lett., 107, 192903 (2015)
15. P. F. Peterson, M. Gutmann, Th. Proffen, S. J. L. Billinge, J. Appl. Cryst., 33, 1192 (2000)
16. T-M. Usher, I. Levin, J. E. Daniels, J. L. Jones, Sci. Reports., 5, 14678 (2015)
17. P. Juhas, T. Davis, C. l. Farrow, S. J. L. Billinge, J. Appl. Cryst., 46, 560 (2013)
18. B. Ravel and M. Newville, J. Synchrotron Radiat., 12, 537 (2005)
19. A. L. Ankudinov, B. Ravel, J. J. Rehr, S. D. Conradson, Phys. Rev. B, 58 [12], 7565-7576 (1998)
20. A. C. Larson and R. B. von Dreele, General Structure Analysis System, Los Alamos National Laboratory Report, LAUR 86-748 (1994)
21. V. Krayzman, I. Levin, J. Woicik, T. Proffen, T. A. Vanderah, M. G. Tucker, J. Appl. Cryst., 42, 867 (2009)
22. V. Krayzman and I. Levin, J. Appl. Cryst., 45, 106-112 (2012)
23. V. A. Shuvaeva, D. Zekria, A. M. Glazer, W. Jiang, S. M. Weber, P. Bhattacharya, P. A. Thomas, Phys. Rev. B., 71 [17], 174114 (2005)
24. D. S. Keeble, E. R. Barney, D. A. Keen, M. G. Tucker, J. Kreisel, P. A. Thomas, Adv. Funct. Mater., 23 [2], 185-190 (2013)
25. E. Aksel, J. S. Forrester, J. C. Nino, K. Page, D. P. Shoemaker, J. L. Jones, Phys. Rev. B., 87 [10], 104113 (2013)
26. I. Levin, V. Krayzman, M. G. Tucker, J. C. Woicik, Appl. Phys. Lett., 104 [24], 242913 (2014)
27. V. Krayzman, I. Levin, J. C. Woicik, Chem. Mater., 19 [4], 932-936 (2007)
28. R.V. Vedrinskii, V.L. Kraizman, A.A. Novakovich, Ph.V. Demekhin, S.V. Urazhdin. J. Phys. Cond. Matter, 10, 9561 (1998)
29. T. R. Welberry, D. J. Goossens, R. L. Withers, K. Z. Baba-Kishi, Metall. Mater. Trans., A41, 1110-1118 (2010)
30. R. L. McGreevy, J. Phys. Cond. Matter, 13, R877-R913 (2001)

31. Y. Okuno and Y. Sakashita, Jpn. J. Appl. Phys., 48, 09KF04 (2009)
32. S. Takagi, A. Subedi, V. R. Cooper, D. J. Singh, Phys. Rev. B., 82, 134108 (2010)
33. H. Wang, B. Wang, Q. Li, Z. Zhu, R. Wang, C. H. Woo, Phys. Rev. B., 75, 245209 (2007)
34. P. Ravindran, R. Vidya, A. Kjekshus, H. Fjellvag, Phys. Rev. B., 74, 224412 (2006)
35. V. V. Svartsman, D. C. Lupascu, J. Amer. Ceram. Soc., 95 [1], 1-26 (2012)
36. A. R. Akbarzadeh, S. Prosandeev, E. J. Walter, A. Al-Barakaty, L. Bellaiche, Phys. Rev. Lett., 257601 (2012)
37. A. Barakaty, S. Prosandeev, D. Wang, B. Dkhil, L. Bellaiche, Phys. Rev. B., 91 214117 (2015)

Acknowledgements

This work has benefited from the use of the Lujan Center at Los Alamos Neutron Science Center, while it was funded by the Department of Energy Office of Basic Energy Sciences. Los Alamos National Laboratory is operated by Los Alamos National Security LLC under DOE contract No DE-AC52-06NA25396. Portions of this research were carried out at the (i) Stanford Synchrotron Radiation Lights Source, a Directorate of the SLAC National Accelerator Laboratory and an Office of Science User Facility operated for the U.S. Department of Energy Office of Science by Stanford University and (ii) National Synchrotron Light Source (NIST beamline X23A2), Brookhaven National Laboratory, supported by the U.S. Department of Energy, Office of Science, Office of Basic Energy Sciences, under Contract No DE-AC02-98CH10886, and (iii) Advanced Photon Source (beamline 11-ID-B). The authors are grateful to J. Siewenie (ORNL) and E. Nelson (SSRL) for their technical assistance with the neutron scattering and X-ray absorption measurements, respectively, and to K. Beyer (APS) for his help with the X-ray PDF measurements.

Appendix A: Automated Assignment of Weights to Individual Datasets during RMC Fits

RMCProfile relies on a Metropolis algorithm to fit calculated signals to data. According to this algorithm, a randomly selected atom is moved in a random direction and a relevant signal is calculated and compared to the data to evaluate the total residual R defined as

$$R = \sum w_i \ \chi_i^2, \qquad (1)$$

where χ_i^2 is the residual associated with the i^{th} dataset (or a set of restraints) and w_i is the weight assigned to this dataset. If the change in R, ΔR, resulting from a given atomic move is negative, this move is accepted unconditionally, while if it is positive (i.e., the fit gets worse), the move is accepted with a probability $e^{-\Delta R}$. After N accepted moves, the probability distribution $F_N(\Delta R)$ for the N+1 move is a bell-like function. A total probability for this N+1 move to be accepted can be expressed as

$$P_N = \int_{-\infty}^{0} F_N(\Delta R) d\Delta R + \int_{0}^{\infty} F_N(\Delta R) e^{-\Delta R} d\Delta R. \qquad (2)$$

Let's modify Equation 1 by introducing a global scale factor T so that

$$\tilde{\tilde{R}} = \sum \frac{w_i'}{T} \chi_i^2, \qquad (3)$$

where w_i' still represents the weight assigned independently to the i^{th} dataset. Replacing ΔR in Equation 2 with $\delta=\widetilde{\widetilde{\Delta R}}$ and keeping w_i' constant, one obtains that for $T\rightarrow\infty$, $P_N\rightarrow 1$ (i.e., all moves are accepted), whereas for $T\rightarrow 0$, $P_N\rightarrow\int_{-\infty}^{0} F_N(\delta) d\delta$ (i.e., only favorable moves are accepted). Thus, the effect of T is analogous to that of temperature in Monte Carlo simulations of thermodynamic equilibrium.

We denote the first and second moments of the distribution $F_N(\delta)$ as Δ_N and σ_N, respectively. During early stages of a typical fit that starts from average atomic positions, Δ_N (and often even $\Delta_N + \sigma_N$) is negative because nearly every move improves the agreement between the calculated and experimental data. As the fit progresses, the distribution curve narrows and shifts in the positive direction while the percentage of accepted moves decreases. A sensible fraction of unfavorable moves is accepted if $\Delta_N + \sigma_N$ is in the range from 15 to 50. In case ($\Delta_N + \sigma_N$) is positive and falls outside of this range, all the weights can be multiplied by a factor 1/T to make ($\Delta_N + \sigma_N$) equal to a desired value L that is specified by the user. If $\Delta_N + \sigma_N$ is negative, most moves are favorable and no changes are needed.

Selecting an optimal combination of weights for multiple datasets is a challenge. As a result, fits frequently become trapped in local minima. Commonly, individual weights require multiple adjustments during a fit which complicates the procedure. We propose an algorithm for automated adjustment of individual weights which ensures that the residuals for all the datasets decrease within a reasonable timeframe, reaching their minimal values preset by a user. RMCProfile saves atomic configurations at specified time intervals. Every time the configuration is saved, we calculate logarithmic derivatives for all the individual components of the total residual as

$$d_i = \frac{\chi_i^2(\mathrm{new}) - \chi_i^2(\mathrm{old})}{n_i(\chi_i^2(\mathrm{new}) + \chi_i^2(\mathrm{old}))/2}, \qquad (4)$$

where $\chi_i^2(\mathrm{new})$ and $\chi_i^2(\mathrm{old})$ refer to the values of the i^{th} residual calculated at times of the current and previous writing of the configuration file, respectively, and n_i is the number of accepted moves during the considered time interval. These derivatives must be negative for the residuals to decrease. Also, a value of the derivative controls the speed with which the corresponding residual is decreasing. We let the user to set the maximum value for each derivative in the ".dat" file that controls the fit. Then, if the residual and its derivative are both larger than their target values, the weight for this dataset is multiplied by a factor greater than unity, which is specified by the user in the ".dat" file. Thus, individual residuals are allowed to increase temporarily but forced to decrease after some period of time.

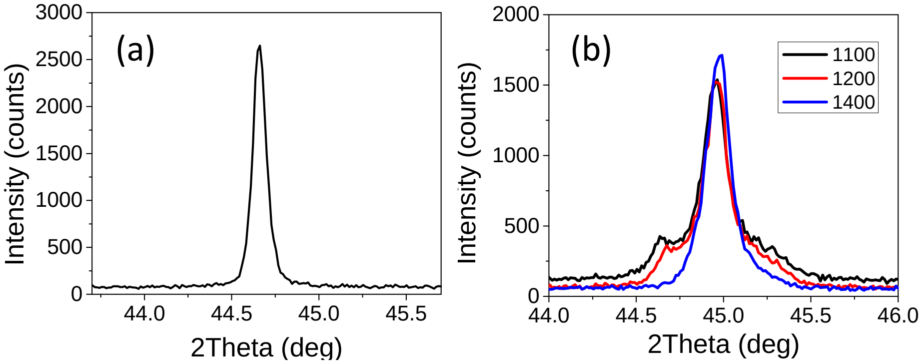
(a)
3000
2500
2000
1500
1000
500
0
Intensity (counts)
44.0
44.5
45.0
45.5
2Theta (deg)
(b)
2000
1500
1000
500
0
Intensity (counts)
1100
1200
1400
44.0
44.5
45.0
45.5
46.0
2Theta (deg)

Fig. 1

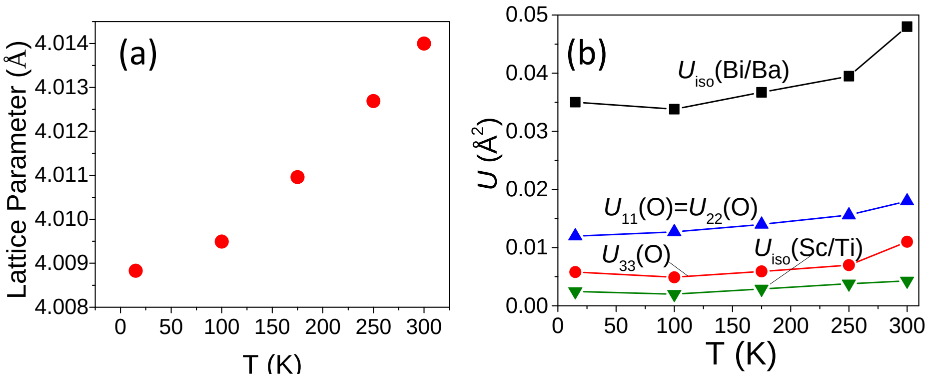
(a)
Lattice Parameter (Å)
4.008
4.009
4.010
4.011
4.012
4.013
4.014
0
50
100
150
200
250
300
T (K)
(b)
U (Å2)
0.00
0.01
0.02
0.03
0.04
0.05
Uiso(Bi/Ba)
U11(O)=U22(O)
U33(O)
Uiso(Sc/Ti)
0
50
100
150
200
250
300
T (K)

Fig. 2

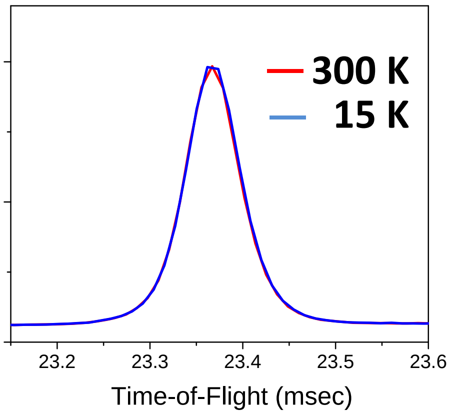

Fig. 3

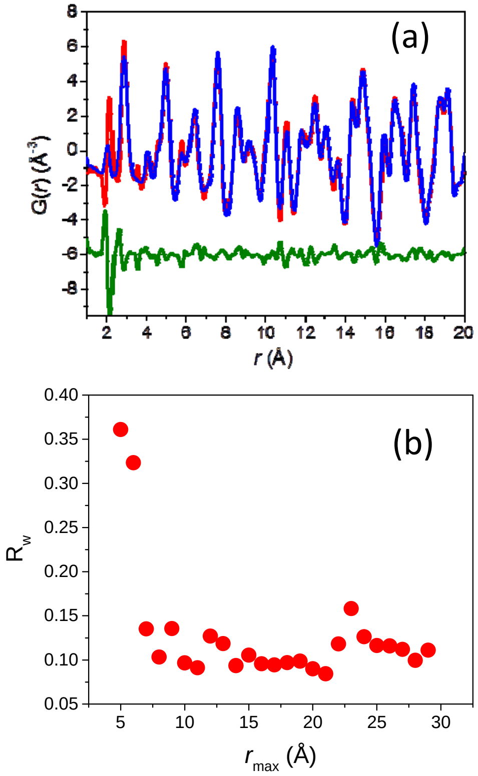
(a)
$G(r)$ (Å^{-3})
8
6
4
2
0
-2
-4
-6
-8
2
4
6
8
10
12
14
16
18
20
r (Å)
(b)
R_w
0.40
0.35
0.30
0.25
0.20
0.15
0.10
0.05
5
10
15
20
25
30
r_{max} (Å)

Fig. 4

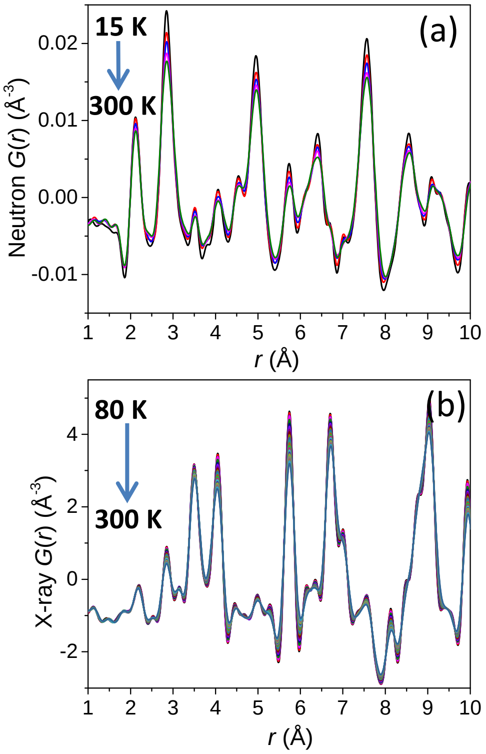
15 K
300 K
(a)
0.02
0.01
0.00
-0.01
Neutron $G(r)$ ($Å^{-3}$)
1
2
3
4
5
6
7
8
9
10
r (Å)
80 K
300 K
(b)
4
2
0
-2
X-ray $G(r)$ ($Å^{-3}$)
1
2
3
4
5
6
7
8
9
10
r (Å)

Fig. 5

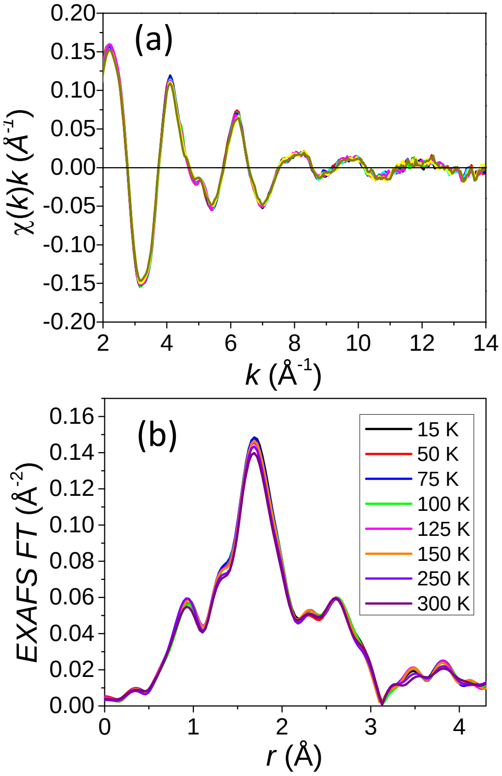
(a)
0.20
0.15
0.10
0.05
0.00
-0.05
-0.10
-0.15
-0.20
χ(k)k (Å-1)
2
4
6
8
10
12
14
k (Å-1)
(b)
0.16
0.14
0.12
0.10
0.08
0.06
0.04
0.02
0.00
EXAFS FT (Å-2)
0
1
2
3
4
r (Å)
15 K
50 K
75 K
100 K
125 K
150 K
250 K
300 K

Fig. 6

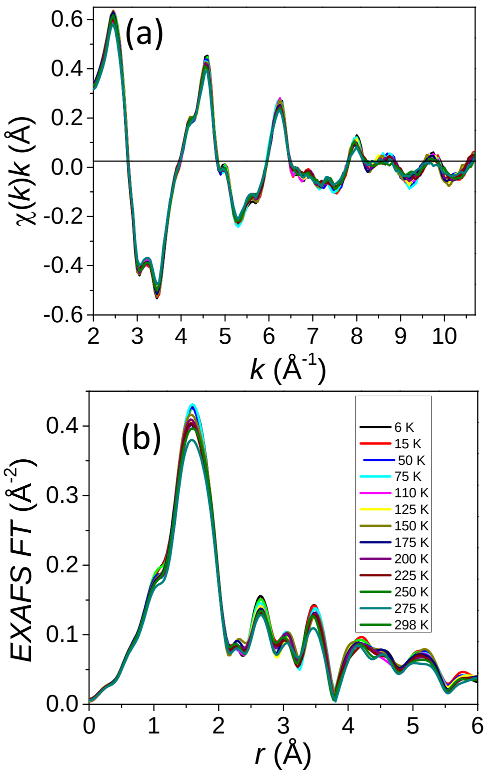
(a)
$\chi(k)k$ (Å)
0.6
0.4
0.2
0.0
-0.2
-0.4
-0.6
2
3
4
5
6
7
8
9
10
k (Å^{-1})
(b)
$EXAFS$ FT (Å^{-2})
0.4
0.3
0.2
0.1
0.0
0
1
2
3
4
5
6
r (Å)
6 K
15 K
50 K
75 K
110 K
125 K
150 K
175 K
200 K
225 K
250 K
275 K
298 K

Fig. 7

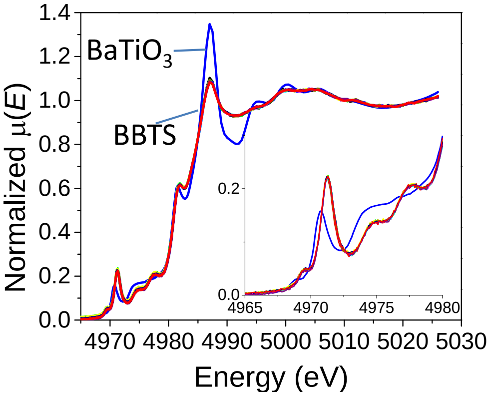
1.4
1.2
1.0
0.8
0.6
0.4
0.2
0.0
Normalized μ(E)
$BaTiO_3$
BBTS
4970
4980
4990
5000
5010
5020
5030
Energy (eV)
0.2
0.0
4965
4970
4975
4980

Fig. 8

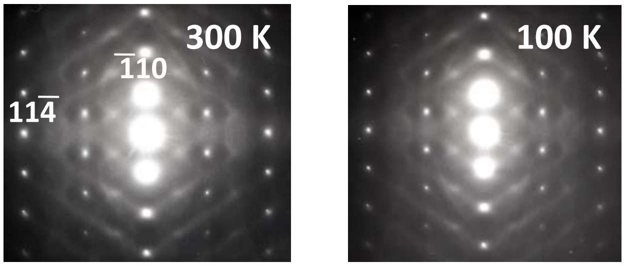

Fig. 9

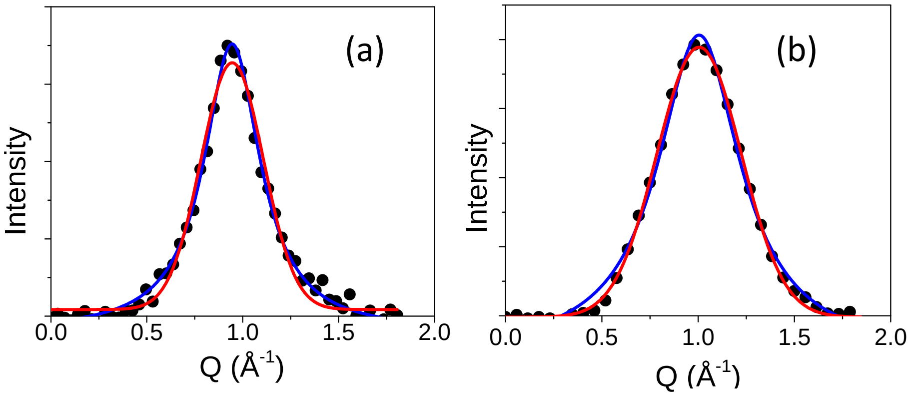

Fig. 10

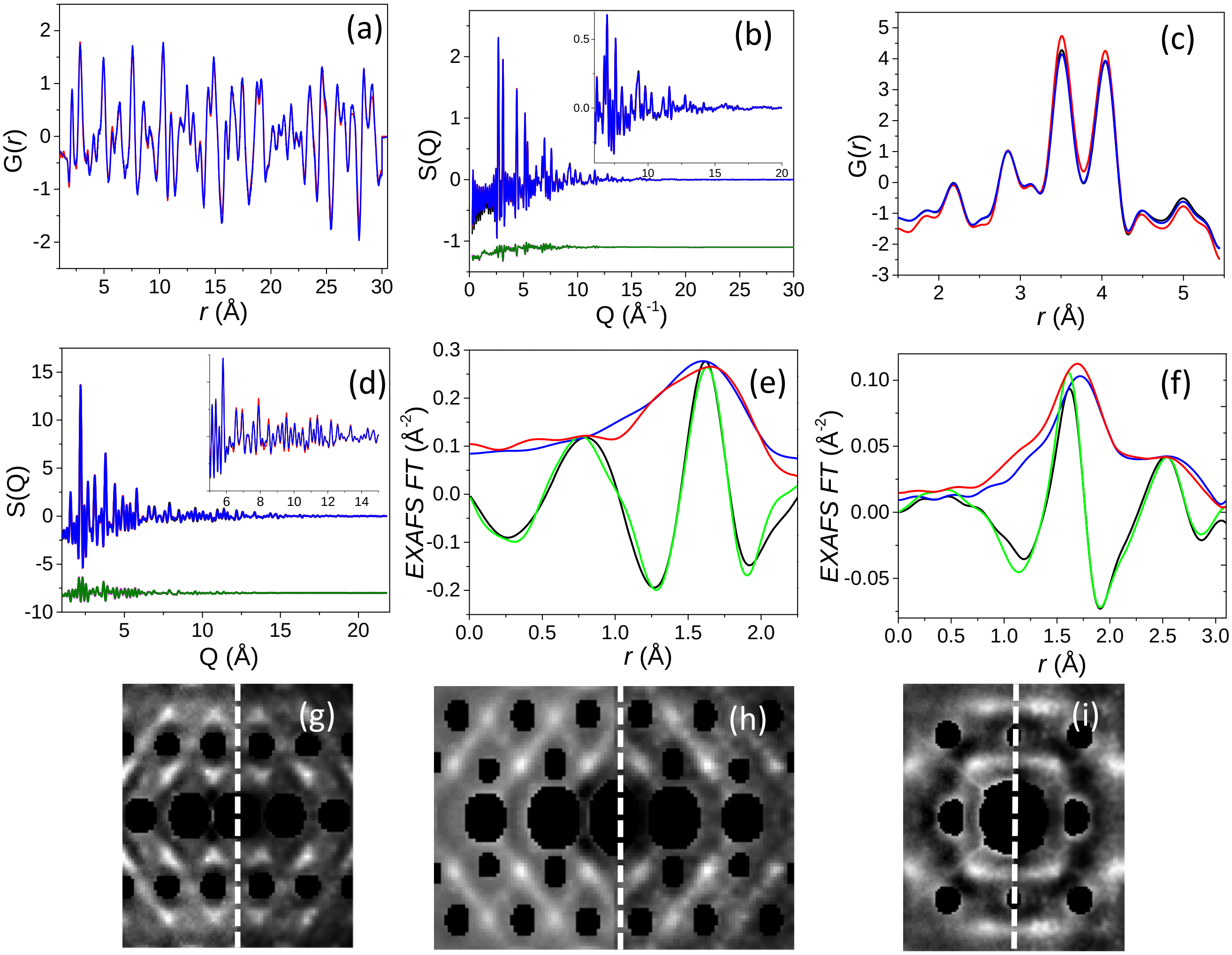

Fig. 11

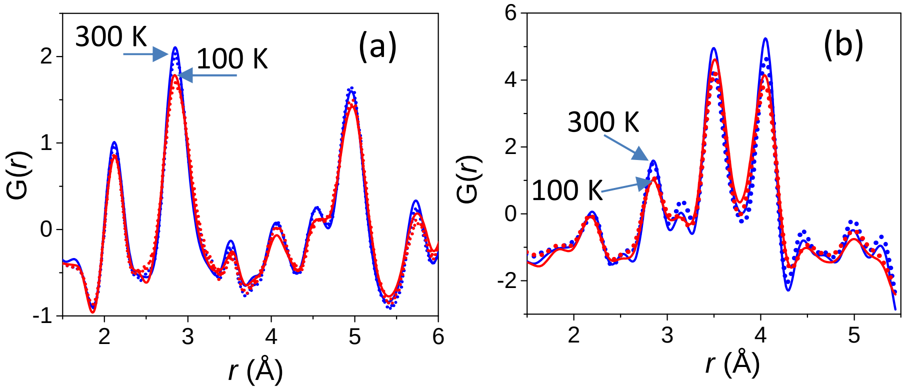

Fig. 12

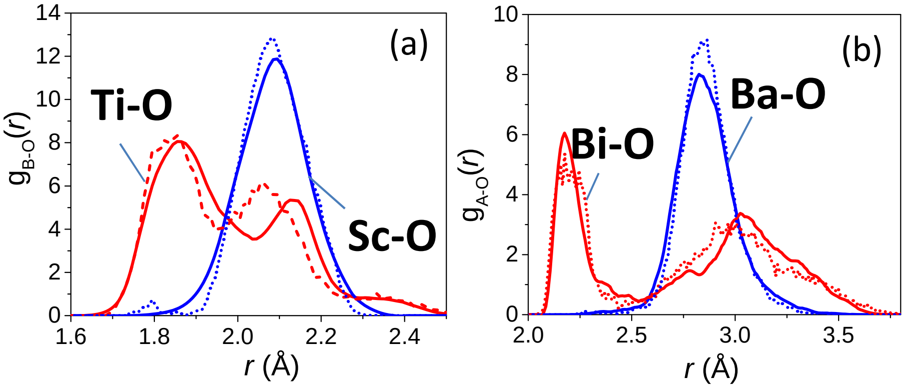
(a)
$g_{B-O}(r)$
0
2
4
6
8
10
12
14
Ti-O
Sc-O
1.6
1.8
2.0
2.2
2.4
r (Å)
(b)
$g_{A-O}(r)$
0
2
4
6
8
10
Bi-O
Ba-O
2.0
2.5
3.0
3.5
r (Å)

Fig. 13

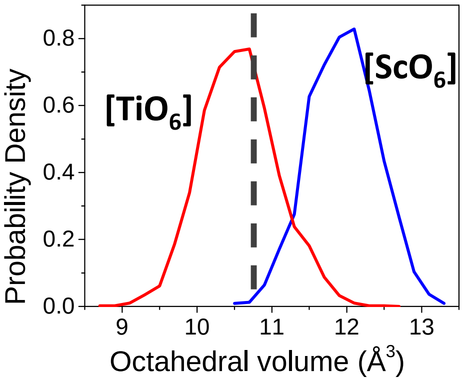

[TiO$_6$]
[ScO$_6$]
Probability Density
0.0
0.2
0.4
0.6
0.8
9
10
11
12
13
Octahedral volume (Å^3)

Fig. 14

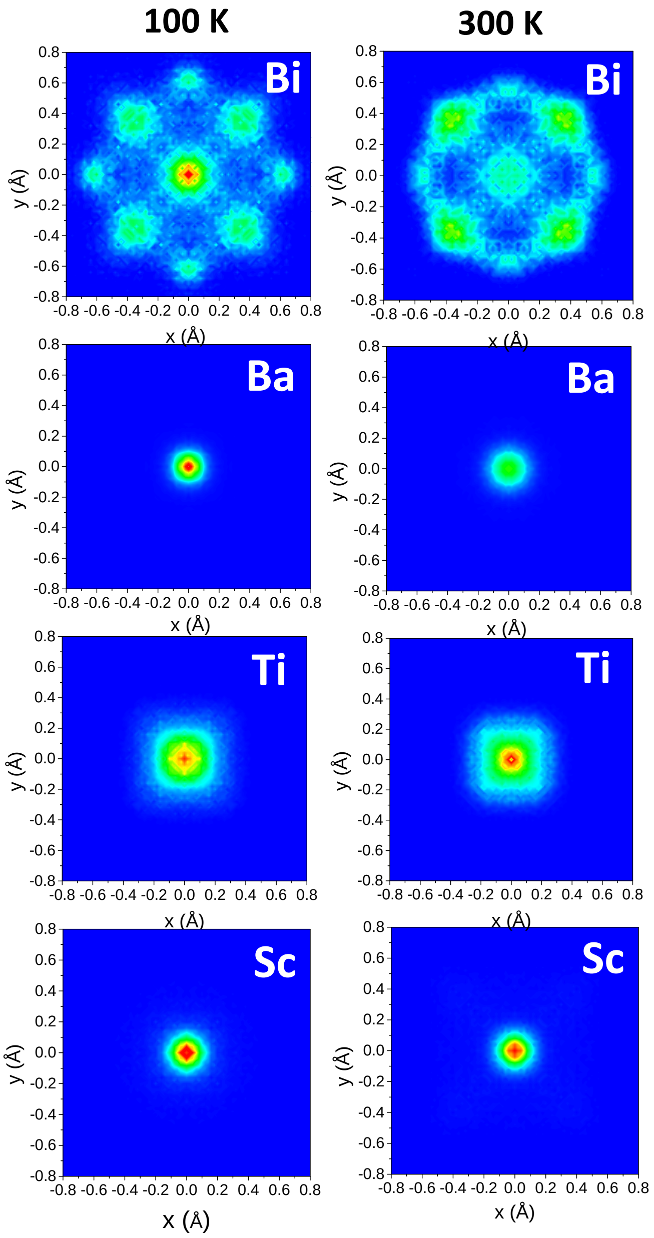
100 K
300 K
Bi
Bi
Ba
Ba
Ti
Ti
Sc
Sc
0.8
0.6
0.4
0.2
0.0
-0.2
-0.4
-0.6
-0.8
y (Å)
-0.8 -0.6 -0.4 -0.2 0.0 0.2 0.4 0.6 0.8
x (Å)

Fig. 15

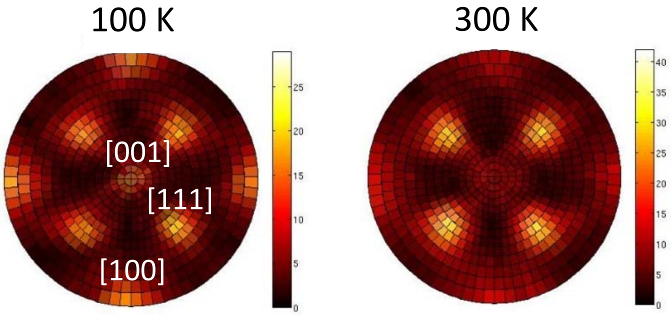

Fig. 16

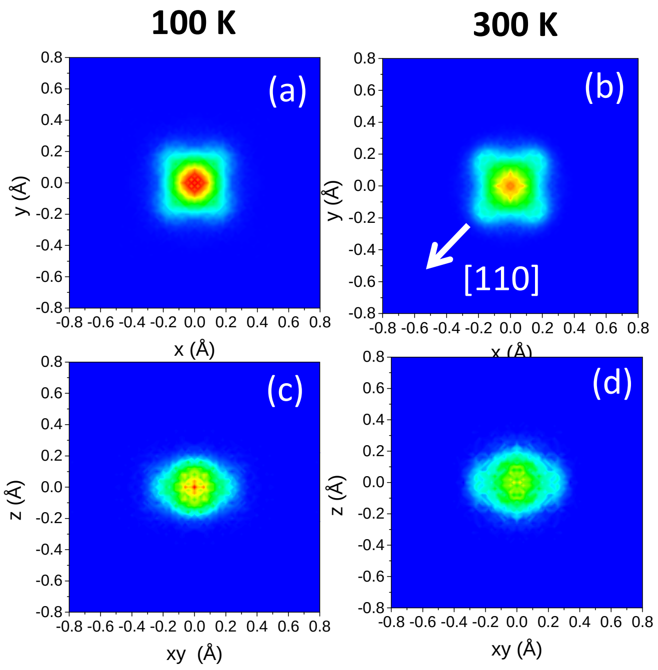
100 K
300 K
(a)
(b)
(c)
(d)
[110]
y (Å)
x (Å)
z (Å)
xy (Å)
0.8
0.6
0.4
0.2
0.0
-0.2
-0.4
-0.6
-0.8
-0.8 -0.6 -0.4 -0.2 0.0 0.2 0.4 0.6 0.8

Fig. 17

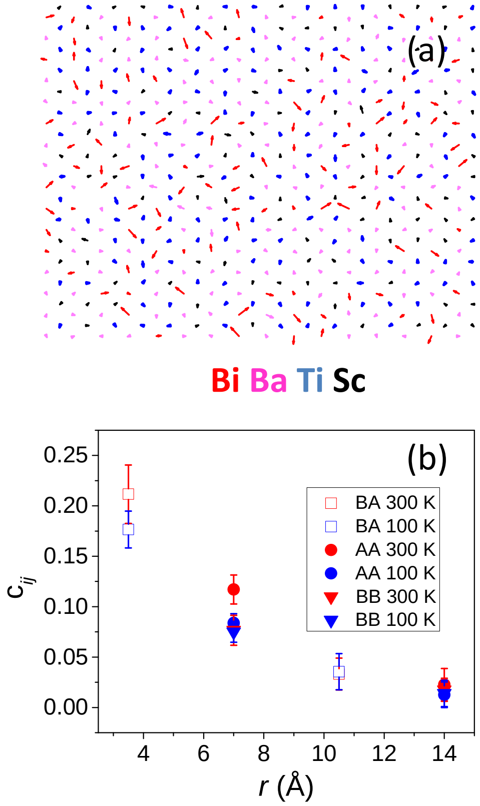
(a)
Bi Ba Ti Sc
(b)
c_{ij}
0.00
0.05
0.10
0.15
0.20
0.25
4
6
8
10
12
14
r (Å)
BA 300 K
BA 100 K
AA 300 K
AA 100 K
BB 300 K
BB 100 K

Fig. 18

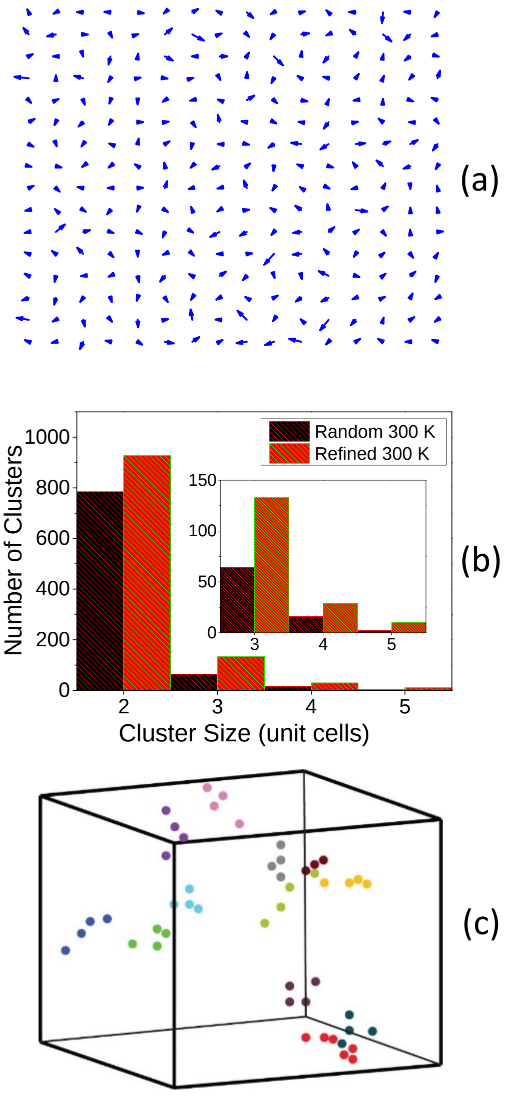
(a)
Number of Clusters
1000
800
600
400
200
0
Random 300 K
Refined 300 K
150
100
50
0
3
4
5
2
3
4
5
Cluster Size (unit cells)
(b)
(c)

Fig. 19

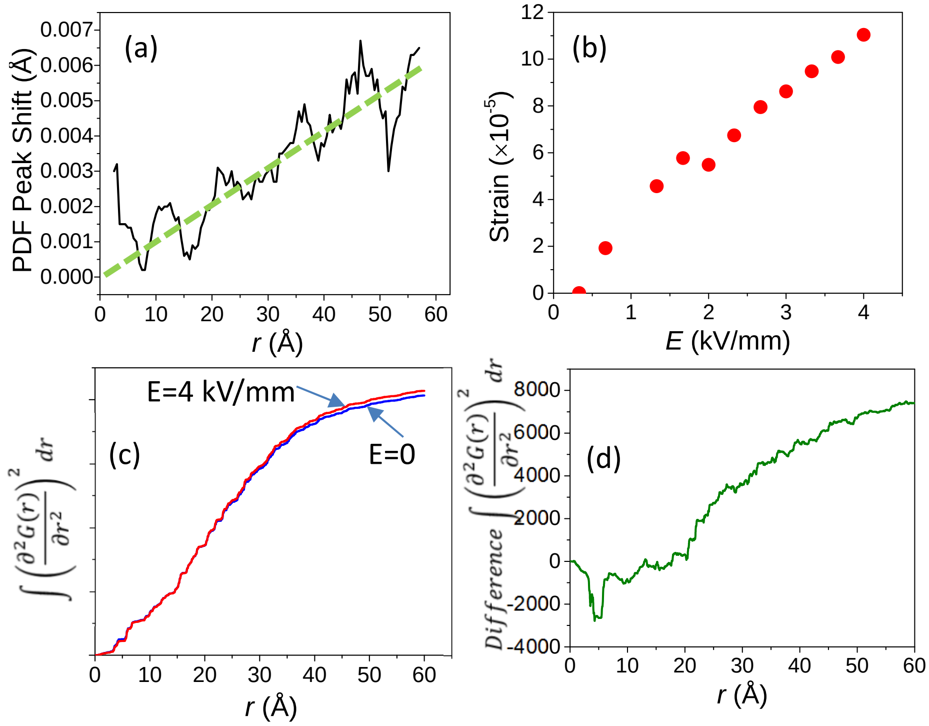

(a)
PDF Peak Shift (Å)
0.000
0.001
0.002
0.003
0.004
0.005
0.006
0.007
0
10
20
30
40
50
60
r (Å)
(b)
Strain (×10^-5)
0
2
4
6
8
10
12
0
1
2
3
4
E (kV/mm)
(c)
$\int \left(\frac{\partial^2 G(r)}{\partial r^2}\right)^2 dr$
E=4 kV/mm
E=0
0
10
20
30
40
50
60
r (Å)
(d)
$Difference \int \left(\frac{\partial^2 G(r)}{\partial r^2}\right)^2 dr$
-4000
-2000
0
2000
4000
6000
8000
0
10
20
30
40
50
60
r (Å)

Fig. 20